Selective Butanol Synthesis over Rhodium−Molybdenum Catalysts Supported in Ordered Mesoporous Silica

Yasuo Izumi,* Kazushi Konishi, Masayasu Tsukahara, Diaa Mosbah Obaid, and Ken-ichi Aika

Department of Environmental Chemistry and Engineering, Interdisciplinary Graduate School of Science and Engineering, Tokyo Institute of Technology, Nagatsuta 4259-G1-16, Midori-ku, Yokohama 226-8502, Japan

Rhodium catalysts were synthesized in ordered mesoporous silica FSM-16 using Rh/Al heteropolyacid anions and/or $[Rh(COD)_2]^+$ complex. The hydroformylation activity of propene was compared to impregnated Rh/FSM-16 catalysts prepared from rhodium chloride. The catalysts were very selective to produce butanols due to the effect of two-dimensional mesoporous reaction space (effective internal pore diameter 27 Å). The selectivity to butanols (*n*-butanol and *i*-butanol) was as much as >98% over $[RhMo_6O_{18}(OH)_6]^{3-}$/FSM-16 catalysts and 73% over $RhCl_3$/FSM-16 catalysts. Under the hydroformylation reaction conditions at 433 K and 60 kPa, 22−28 Å of supported nanoparticles were present based on Rh K-edge extended X-ray absorption fine structure (EXAFS) and high-resolution transmission electron microscopy (HR TEM) measurements. Rh metallic nanoparticles atomically mixed with Mo atoms and distorted heteropolyacid species coexisted in the $[RhMo_6O_{18}(OH)_6]^{3-}$/FSM-16 catalysts based on Rh and Mo K-edge EXAFS and HR TEM measurements. The population of metallic nanoparticles increased as the metal loading amount decreased from 5.2 to 0.22 wt % Rh. Thus, metallic nanoparticles in FSM-16 were essential for the butanol synthesis and Mo played an additional promoter role to increase the selectivity further. A reaction mechanism was proposed in which the metallic nanoparticle surface was predominantly adsorbed with CO and multiple-step hydrogenations of oxygenate intermediates proceeded to form butanols during slow diffusion in the two-dimensional mesoporous space.

Introduction

The homogeneous-phase hydroformylation of propene is one of the major industrial processes to produce butanal using rhodium catalysts ligated with $P(C_6H_5)_3$ group(s).[1] Major practical problems of homogeneous catalytic processes are separation and stability. Recently, technical solutions for the separation problem were reported to utilize a polymer ligand soluble in the reactants but insoluble in the product. Supercritical CO_2 and ionic liquids dissolve the reactants and Rh catalysts, but the produced aldehyde was separated when the density of CO_2 decreased from supercritical conditions.[1]

Heterogeneous hydroformylation reactions of hexene and octene were reported to proceed over the $HRh^I(CO)(PPh_3)_3$ complex supported in/on a micro-/mesoporous NaY zeolite, MCM-41, and MCM-48 crystallines to produce aldehydes.[2] The $[Rh^ICl(CO)_2]_2$ complex was anchored via silane groups terminated with phosphine, amine, or a thiol group grafted to MCM-41.[3] The Rh catalysts anchored via an amine were stable and recyclable in the cyclohexene hydroformylation to produce cyclohexane carboxaldehyde. The $Rh(CO)_2(acac)$ (acac = acetylacetonate) complex anchored to trisulfonated triphenylphosphine and the phosphinated $[RhCl(1,5-COD)]_2$ (COD = cyclooctadiene) complex were immobilized in MCM-41 and used for hexene hydroformylation.[4,5]

In this study, the Anderson-type, flat pillbox-shaped heteropolyacid anion molecule[6] $[AlMo_6O_{18}(OH)_6]^{3-}$ was used as an anchor for the $[Rh^I(COD)_2]^+$ cation in FSM-16 [effective pore diameter: 27 Å (10 Å = 1 nm)] for propene hydroformy-

lation. Rh complexes were immobilized in/on MCM-41[7] and a NaY zeolite[8] using Keggin-type $H_3PW_{12}O_{40}$ molecules.[7−9] The heterogenized catalysts were applied for the styrene derivatives hydroformylation[7] and enantioselective hydrogenation reactions.[8] The Rh complexes were also immobilized using heteropolyacid anions on alumina,[10] carbon,[10] or montmorillonite[11] for selective hydrogenation reactions. The activity loss was minimal with the supporting Rh complexes anchored with heteropolyacid when compared to the direct impregnation in/on meso-/microporous supports.

A binary oxide $[NH_4]^+_3[Rh^{III}Mo_6O_{18}(OH)_6]^{3-}$ crystal[6] **1** was also supported in/on FSM-16. Catalytic performance of the Rh−Mo catalysts was compared to conventional, impregnated Rh/FSM-16 derived from $RhCl_3$ and $[Rh^I(COD)_2]^+$ directly immobilized in/on FSM-16. Promoted butanol formation was reported over $Rh-Mo/SiO_2$ catalysts in the propene hydroformylation.[12,13] The requisites for selective butanol synthesis were suggested to be the combination of two-dimensional mesoporous space and Rh nanoparticles atomically mixed with Mo.

Methods

Catalysts Synthesis/Preparation. Crystal **1** was synthesized by adding $Rh(NO_3)_3$ (Kanto, 1.6 mmol) to an aqueous solution of $[NH_4]^+_6[Mo_7O_{24}]^{6-}$ (Wako, special grade, 2.1 mmol) at 373 K.[6] The reaction mixture was cooled to 290 K and filtered. The obtained crystal powder was dried in air. FSM-16 was from Fuji Silysia Chemical Ltd. and was used as received. The crystal **1** was dissolved in a minimal amount of distilled, deionized water and reacted with FSM-16 at 290 K for 12 h using a magnetic stirrer. Then, the solvent was evaporated. The obtained orange powder is denoted as $[RhMo_6O_{18}(OH)_6]^{3-}$/FSM-16.

* To whom correspondence should be addressed. Phone and Fax: +81-45-924-5569. E-mail: izumi.y.ac@m.titech.ac.jp.

TABLE 1: Basic Physicochemical Data for Various Rhodium−Molybdenum Catalysts Supported in/on FSM-16, Reference Rh Catalysts, and FSM-16

particle entry		Rh (wt %)	Cl (wt %)[a]	specific surface area (m²g⁻¹)	pore radius (Å)[b]	pore volume (mm³ g⁻¹)[b]	d_{100}-spacing (Å)[c]	mean size (Å)[d]
a	$[RhMo_6O_{18}(OH)_6]^{3-}$/FSM-16	0.22		1126 (1234)[e]	12.1 (12.1)[e]	873 (889)[e]	37.8 (37.8)[e]	f
b		3.0		923 (930)[e]	11.2 (11.7)[e]	786 (813)[e]	37.7	24 (±0.4)
								28 (±5.5)[e]
c		5.2		814	10.8	715	37.8	
d	$[Rh(COD)_2]^+ - [AlMo_6O_{18}(OH)_6]^{3-}$/FSM-16	1.6		642	10.7	678	37.5	
e	RhCl₃/FSM-16	0.5	0.28 (±0.14)					22 (±0.4)[e]
f		3.0	0.22 (±0.13)	738[e]	11.4[e]	170[e]	38.8	
g		33		633[e]	10.2[e]	145[e]	37.4	28 (±9.3)[e]
h	FSM-16			1274	13.5	904	36.8	

[a] Based on EPMA measurements, after pretreatment in H₂ (673 K). [b] Based on DH plots. [c] Based on XRD measurements. [d] Based on high-resolution TEM measurements. [e] Data for catalyst after hydroformylation reaction (433 K, 5 h). [f] Metal particles were difficult to detect.

$[NH_4]^+_3[Al^{III}Mo_6O_{18}(OH)_6]^{3-}$ crystal **2** was synthesized[6] in a similar manner to the route for crystal **1** and impregnated in/on FSM-16 similar to the route for $[RhMo_6O_{18}(OH)_6]^{3-}$/FSM-16. The $[Rh^I(COD)_2]^+[BF_4]^-$ crystal **3** was synthesized from $[RhCl(COD)]_2$ (Wako), 1,5-COD (Wako, >98%), and AgBF₄ (Wako, >97%).[14] The obtained dark red crystal powder was dissolved in distilled ethanol in an argon atmosphere and mixed with $[AlMo_6O_{18}(OH)_6]^{3-}$/FSM-16 at 290 K for 12 h. The mixture was filtered, and the powder was washed several times until the filtrate became colorless, i.e., the UV-visible absorption peak derived from compound **3** disappeared. The obtained yellow powder is denoted as $[Rh(COD)_2]^+ - [AlMo_6O_{18}(OH)_6]^{3-}$/FSM-16.

The ethanol solution of crystal **3** was mixed with FSM-16 in an Ar atmosphere similar to that for $[Rh^I(COD)_2]^+ - [AlMo_6O_{18}(OH)_6]^{3-}$/FSM-16. The obtained sample was denoted as $[Rh^I(COD)_2]^+$/FSM-16. RhCl₃·3H₂O (Wako, >95%) was impregnated in/on FSM-16 from the aqueous solution. This catalyst is denoted as RhCl₃/FSM-16. Rh loading was varied between 0.22 and 5.2 wt % in all the catalysts above, except that 33 wt % of Rh was impregnated from RhCl₃ to check the maximum Rh loading in the mesopore of FSM-16.

Propene Hydroformylation Measurements. Hydroformylation reactions of propene were carried out in a Pyrex glass closed circulation system (effective internal volume 132 cm³). The typical catalyst volume used was 0.20 g. All of the catalyst characterization was performed with sample treatments/kinetic measurements in this system followed by transfer to each cell utilizing the Schlenk technique without contact to air except for sample loading on the TEM and XRD apparatus.

$[RhMo_6O_{18}(OH)_6]^{3-}$/FSM-16, $[Rh(COD)_2]^+ - [AlMo_6O_{18}(OH)_6]^{3-}$/FSM-16, and $[Rh(COD)_2]^+$/FSM-16 catalysts were evacuated (<10⁻⁶ Pa) at 290 K for 2 h prior to tests. RhCl₃/FSM-16 catalysts were heated in hydrogen (27 kPa) at 673 K for 1 h and evacuated at 673 K for 30 min before tests. Relatively severe pretreatment for the latter catalysts was done to remove chlorine (0.22−0.28 wt % of Cl after pretreatment, Table 1). A total pressure of 60 kPa of C₃H₆, CO, and H₂ (molar ratio 1:1:1) was introduced to the reaction system at 413−453 K. The flow rate was 90 cm³ min⁻¹. The conversion and product distribution did not change significantly when the rate varied in the range 60−120 cm³ min⁻¹. Produced propane, *n*-butanal, *i*-butanal, *n*-butanol, and *i*-butanol were analyzed by a TCD gas chromatograph (Shimadzu GC-8A) equipped with separation columns of Porapak Q (3 m) and active carbon (2 m).

XRD, Sorption/Desorption Isotherms, TEM, and EPMA Measurements. X-ray diffraction (XRD) data were obtained using the Multiflex-S diffractometer (Rigaku). Cu Kα emission was used with a Ni filter. The diffractions were monitored in

the $2\theta_B$ range of 2−70° (θ_B, Bragg angle). The BET specific surface area (SA) was measured at 77 K using BELSORP Mini (Bell Japan) with N₂ as an adsorbate. The samples were evacuated at 383 K for 1 h before measurements. Transmission electron microscope (TEM) and electron probe microanalysis (EPMA) observations were performed using the field-emission-type JEM-2010F at an accelerating voltage of 200 kV (JEOL) and JXA-8100 (JEOL), respectively, at the Center of Advanced Materials Analysis (CAMA), Tokyo Institute of Technology (Dr. A. Genseki). The sample powder was dispersed in carbon tetrachloride using ultrasound and mounted on a carbon-coated Cu grid (TEM) or pressed as a disk (EPMA).

EXAFS Measurements and Analyses. The incipient catalyst samples were evacuated (<10⁻⁶ Pa) at 290 K for 2 h and transferred to a Pyrex glass cell. The windows were sealed with Kapton film of 12.5 μm in thickness. Sample thickness was controlled to give a Rh and Mo K absorption edge jump of 1 for Rh and Mo K-edge measurements.

The Rh and Mo K-edge extended X-ray absorption fine structure (EXAFS) spectra were measured at 30−290 K in transmission mode at beamlines 10B of the Photon Factory (PF) and NW10A of the Photon Factory advanced ring (PF-AR) at the High Energy Accelerator Research Organization (KEK). The PF and PF-AR storage ring energy was 2.5 and 6.5 GeV, respectively, and the ring current was 310−260 mA and 57−33 mA, respectively. A Si(311) double crystal monochromator was used. The detail of the focusing cylindrical mirror system of NW10A was in ref 15. Ar and Kr gases were purged in the I_0 and I_t ion chambers, respectively. The rising edge energy of Rh and Mo metal was calibrated at 23 219.8 and 20 003.9 eV, respectively.[16] The scan steps were ≈9, ≈0.5, and 1.0−1.5 eV for the preedge, near edge, and EXAFS regions, respectively. The accumulation time for each data point was 1−10 s.

The EXAFS data analysis was performed using XDAP version 2.2.7 (XAFS Services International) based on the works of M. Vaarkamp, H. Linders, and D. Koningsberger. Multiple shell analyses were performed for the Fourier-filtered k^3-weighted EXAFS data in *k*- and *R*-space using empirical parameters extracted from EXAFS for Rh₂O₃, crystal **3**, Rh metal, crystal **1**, K₂MoO₄, and crystal **1** for Rh−O, Rh−C, Rh(−C−)C, Rh−Rh, Rh(−O)Mo, Mo−O, and Mo(−O−)Mo bonds, respectively. The bond distances and coordination numbers (N) of these references were summarized in Table 2 based on crystal structure data for Rh metal, Rh₂O₃, crystals **1** and **3**, and K₂MoO₄.[17-20] The model parameters for the Mo−Rh bond were theoretically generated using FEFF version 8.2 (Table 2).[21] The σ^2 values were relative to those for references. The many-body reduction factor S_0^2 was assumed to be equal for the sample and reference. The goodness of fit was given as

TABLE 2: Empirical (A) and Theoretical (B) Fit Parameters Information for Rhodium and Molybdenum K-edge EXAFS Analyses

| | | model | | data range used | | |
		R (Å)	N	k (Å^{-1})	R (Å)	reference
shell	compound					
		(A) Empirical				
Rh−O	Rh$_2$O$_3$	2.05	6	3.56−18.32	1.37−1.95	17
Rh−C	[Rh(COD)$_2$]$^+$[BF$_4$]$^-$	2.228	8	3.45−15.50	1.58−2.10	18
Rh(−C−)C	[Rh(COD)$_2$]$^+$[BF$_4$]$^-$	3.043	8	3.45−15.50	2.30−2.84	18
Rh−Rh	Rh metal	2.689	12	2.58−20.38	2.12−2.67	17
Rh(−O−)Mo	[NH$_4$]$^+$$_3$[RhMo$_6O_{18}(OH)_6$]$^{3-}$	3.355	6	2.57−12.88	2.75−3.37	19
Mo−O	K$_2$MoO$_4$	1.76	4	3.37−19.30	1.25−1.63	20
Mo(−O−)Mo	[NH$_4$]$^+$$_3$[RhMo$_6O_{18}(OH)_6$]$^{3-}$	3.366	3	3.45−13.70	2.48−3.38	19
		(B) Theoretical				
Mo−Rh	(FEFF 8.2)	2.689	12	1.72−19.65	2.13−2.68	21

TABLE 3: Results of Propene Hydroformylation Reaction at 433 K^a for 5 h over Various Rhodium−Molybdenum Catalysts Supported in/on FSM-16 and Reference Rh Catalysts

(A)

| | | | | | selectivity (mol %) | | | | |
entry		Rh (wt %)	Mo/Rh atomic ratio^b	conversion (%)	C$_3$H$_8$	n-C$_3$H$_7$CHO	i-C$_3$H$_7$CHO	n-C$_4$H$_9$OH	i-C$_4$H$_9$OH
a	[RhMo$_6$O$_{18}$(OH)$_6$]$^{3-}$/FSM-16	0.22	6	0.27	<0.7	<0.7	<0.7	62	38
b		1.0	6	0.13	19	<0.7	<0.7	81	<0.7
c		3.0	6	0.52	3.0	<0.7	<0.7	97	<0.7
d		5.2	6	0.40	2.7	16	22	60	<0.7
e	[Rh(COD)$_2$]$^+$-[AlMo$_6$O$_{18}$(OH)$_6$]$^{3-}$/FSM-16	1.6	9	1.33	29	34	8.0	<0.7	29
f	[Rh(COD)$_2$]$^+$/FSM-16	1.1		1.55	91	5.8	3.6	<0.7	<0.7
g	RhCl$_3$/FSM-16	0.50		0.30	10	<0.7	16	73	<0.7
h		3.0		0.91	1.2	23	24	39	13
i		33		1.61	40	11	2.9	25	21

(B)

| | | | specific reaction rate (10^{-3} mol$_{product}$ mol$_{Rh}^{-1}$ h^{-1})^c | | | | |
entry		Rh (wt %)	C$_3$H$_8$	n-C$_3$H$_7$CHO	i-C$_3$H$_7$CHO	n-C$_4$H$_9$OH	i-C$_4$H$_9$OH
a	[RhMo$_6$O$_{18}$(OH)$_6$]$^{3-}$/FSM-16	0.22	<0.5	<0.5	<0.5	41	26
b		1.0	1.3	<0.1	<0.1	5.6	<0.1
c		3.0	0.3	<0.1	<0.1	9.2	<0.1
d		5.2	0.1	0.7	0.9	2.5	<0.1
e	[Rh(COD)$_2$]$^+$−[AlMo$_6$O$_{18}$(OH)$_6$]$^{3-}$/FSM-16	1.6	13	15	3.6	<0.1	13
f	[Rh(COD)$_2$]$^+$/FSM-16	1.1	70	4.5	2.8	<0.1	<0.1
g	RhCl$_3$/FSM-16	0.50	3.3	<0.2	5.4	24	<0.2
h		3.0	0.2	3.8	3.9	6.5	2.1
i		33	1.1	0.3	0.1	0.7	0.6

^{a} Initial total gas pressure 60.0 kPa; propene/CO/H$_2$ = 1:1:1. ^{b} Evaluated based on the edge jump values of Rh and Mo K-edge X-ray absorption using a spline function. ^{c} Average reaction rate for 5 h of reaction.

requested by the Committee on Standards and Criteria in X-ray Absorption Spectroscopy.

Results

Propene Hydroformylation. The catalytic test results in propene + CO + H$_2$ at 433 K were summarized in Table 3 and the time courses were depicted in Figure 1 for supported Rh−Mo catalysts and reference Rh catalysts. For the RhCl$_3$/FSM-16 catalyst with a Rh loading of 33 wt %, the major product was propane (Table 3, part A, entry i).[22] As the Rh loading decreased from 33 to 0.50 wt %, the specific reaction rates both for propane and for n-butanol formation increased (part B of Table 3) and the latter increase was greater. As a balance, the selectivity to butanols increased to 73 mol % (entries g−i in part A of Table 3).

When compound **1** was used as a catalyst precursor, butanols selectivity was even greater (60−98 mol %, Table 3, entries a−d). The specific reaction rates [(2.5−67) × 10^{-3} mol$_{product}$ mol$_{Rh}^{-1}$ h^{-1}] to butanols were comparable to those over RhCl$_3$/FSM-16 catalysts [(1.3−24) × 10^{-3} mol$_{product}$ mol$_{Rh}^{-1}$ h^{-1}]. The nature of using the precursor **1** anion suppressed the simple hydrogenation of propene: 0.7−19 mol % and, accordingly,

the selectivity to butanols further increased for [RhMo$_6$O$_{18}$-(OH)$_6$]$^{3-}$/FSM-16. The conversion was greatest when the Rh loading was 3.0 wt % (Table 3, part A, entry c). The n- and i-butanal formation was negligible over [RhMo$_6$O$_{18}$(OH)$_6$]$^{3-}$/FSM-16 catalysts with a Rh loading of 0.22−3.0 wt %, similar to refs 12 and 13. Repeated hydroformylation tests (3 times) for 5 h were performed for the [RhMo$_6$O$_{18}$(OH)$_6$]$^{3-}$/FSM-16 catalyst with 3.0 wt % Rh by evacuating the catalyst at 433 K between each test. Significant change was not found in the conversion and selectivity to each product.

The trend of time course was in contrast between [RhMo$_6$O$_{18}$-(OH)$_6$]$^{3-}$/FSM-16 and RhCl$_3$/FSM-16 catalysts. The catalytic performance of supported Rh heteropolyacid catalysts was persistent. Typically, the formation rates of each product were constant for the catalyst of 5.2 wt % Rh (Figure 1c). In contrast, products switching was observed at 1.5−2 h from n-butanol and i-butanol to n-butanal and/or i-butanal over RhCl$_3$/FSM-16 catalysts (Figure 1f,g).

When compound **3** cation was heterogenized using compound **2** anion as an anchor to FSM-16, the major products were n-butanal, propane, and i-butanol all in a similar selectivity (Table 3e). Over [Rh(COD)$_2$]$^+$/FSM-16 in the absence of
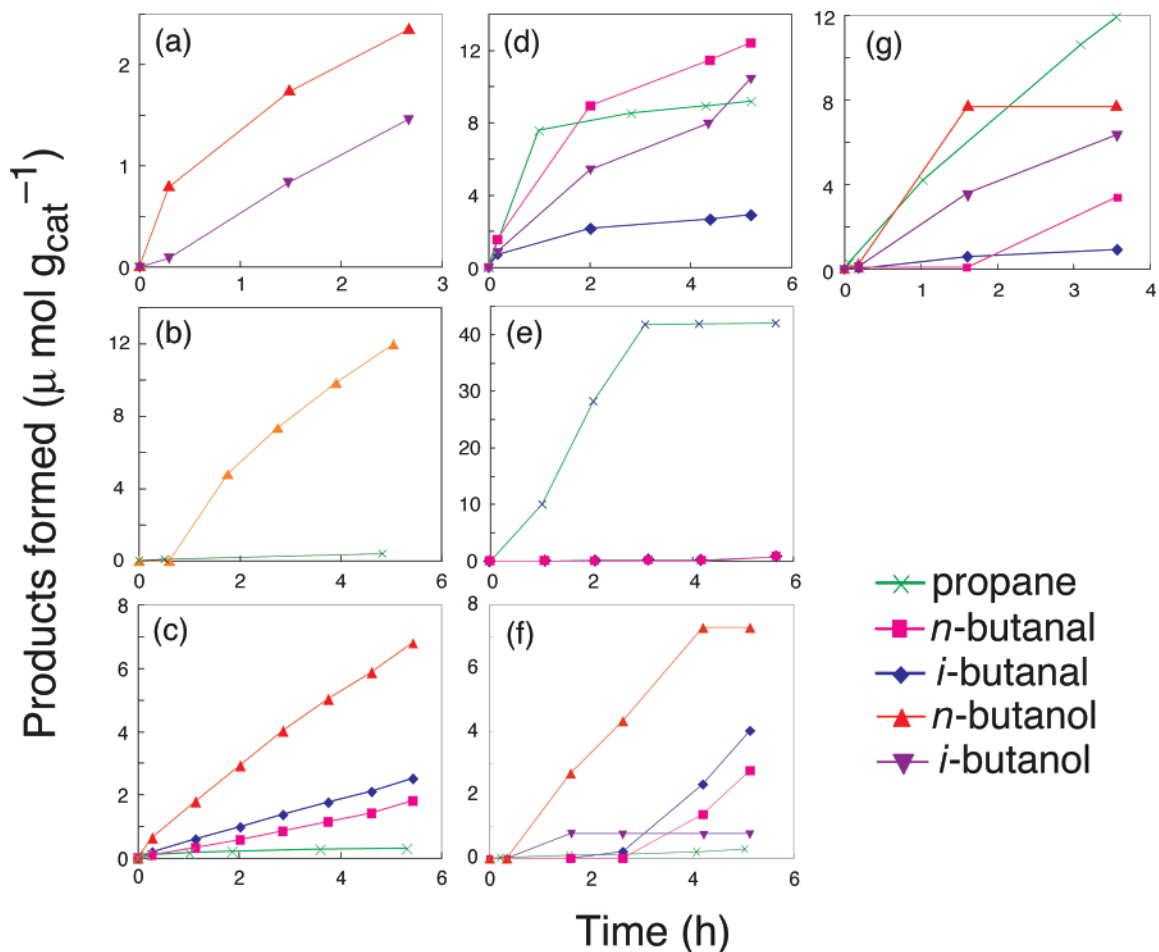
Figure 1. Time courses of propene hydroformylation reaction at 433 K over $[RhMo_6O_{18}(OH)_6]^{3-}$/FSM-16 [(a) 0.22, (b) 3.0, and (c) 5.2 wt % Rh], (d) $[Rh(COD)_2]^+-[AlMo_6O_{18}(OH)_6]^{3-}$/FSM-16, (e) $[Rh(COD)_2]^+$/FSM-16, and $RhCl_3$/FSM-16 catalysts [(f) 3.0 and (g) 33 wt % Rh]. Products: × propane, ■ *n*-butanal, ◆ *i*-butanal, ▲ *n*-butanol, and ▼ *i*-butanol.

compound **2**, propane was the major product (91 mol %) in addition to 9.4 mol % of butanals (Table 3, entry f).

Basic Physicochemical Characterization of Rh[−Mo] Catalysts. Basic physicochemical data were summarized in Table 1 for supported Rh−Mo catalysts and reference Rh catalysts. The specific surface area (SA) for FSM-16 (1274 m² g⁻¹) decreased by 12−36% upon supporting crystal **1** (Table 1, entries a−c). The decrease for the sample of 0.22 wt % Rh may be trivial because the specific SA increased by 10% after the hydroformylation reaction (Table 1, entry a). The pore radius and volume decreased by 10−20% and 1.7−21%, respectively, upon supporting crystal **1** and/or the hydroformylation tests. The specific SA decreased to 50−58% upon supporting crystals **3 + 2** or $RhCl_3$. The pore volume detrimentally became only 16−19% for $RhCl_3$/FSM-16 catalysts compared to data for FSM-16.

The change of d_{100} spacing values was monitored by XRD based on the two-dimensional hexagonal symmetry of FSM-16. The d_{100} value increased by 2.4−2.7, 1.9, and 1.6−5.4% upon supporting compound **1**, compounds **3 + 2**, and $RhCl_3$, respectively (Table 1). The (100) peak height (diffracted X-ray counts per second) decreased by 8.1−72% upon supporting crystal **1**. The FSM-16 matrix may swell up during the supporting procedure in aqueous solution. The gradual decreases of specific SA, pore radius, and pore volume as the metal loading increased should be the geometrical (blocking) effect of compounds **1**, **3 + 2**, or $RhCl_3$.

The pore radius and d_{100} spacing values based on the adsorption/desorption method and XRD, respectively, were compared to mean metallic particle size based on TEM measurements (Table 1 and Figures 2 and 3). Obtained values from TEM were 24−28 and 22−28 Å for $[RhMo_6O_{18}(OH)_6]^{3-}$/FSM-16 (3.0 wt % Rh, Figure 3A,B) and $RhCl_3$/FSM-16 catalysts (0.5−33 wt %, Figure 3C). Thus, the major part of supported particles can be accommodated in the effective pore of 27 Å of FSM-16 (Figure 2) when the Rh loading was less than 3 wt % and before catalysis. The mean nanoparticle size increased by 4 Å after hydroformylation tests (Figure 3B and Table 3, entry b) for the $[RhMo_6O_{18}(OH)_6]^{3-}$/FSM-16 catalyst. As the Rh loading decreased from 33 to 0.5 wt %, the mean nanoparticle size decreased by 6 Å for the $RhCl_3$/FSM-16 catalysts. In the TEM image, particles exterior to the FSM-16 mesopore were minor (Figure 3) except for the $RhCl_3$/FSM-16 catalyst with 33 wt % Rh.

Rh and Mo K-edge EXAFS for Supported Rh[−Mo] Catalysts. Rh and Mo K-edge EXAFS spectra were measured for Rh[−Mo]/FSM-16 catalysts before and after propene hydroformylation tests. The best-fit values were summarized in Tables 4 and 5, respectively. Relative Debye Waller factors and fit errors were listed in more detailed versions (Tables S1 and S2).

a. Rh K-Edge. For $[RhMo_6O_{18}(OH)_6]^{3-}$/FSM-16 catalysts, an intense peak was observed at 1.4−1.6 Å (Supporting Information, Figure S1, part B, spectra a1, b1, and c1) in the Fourier
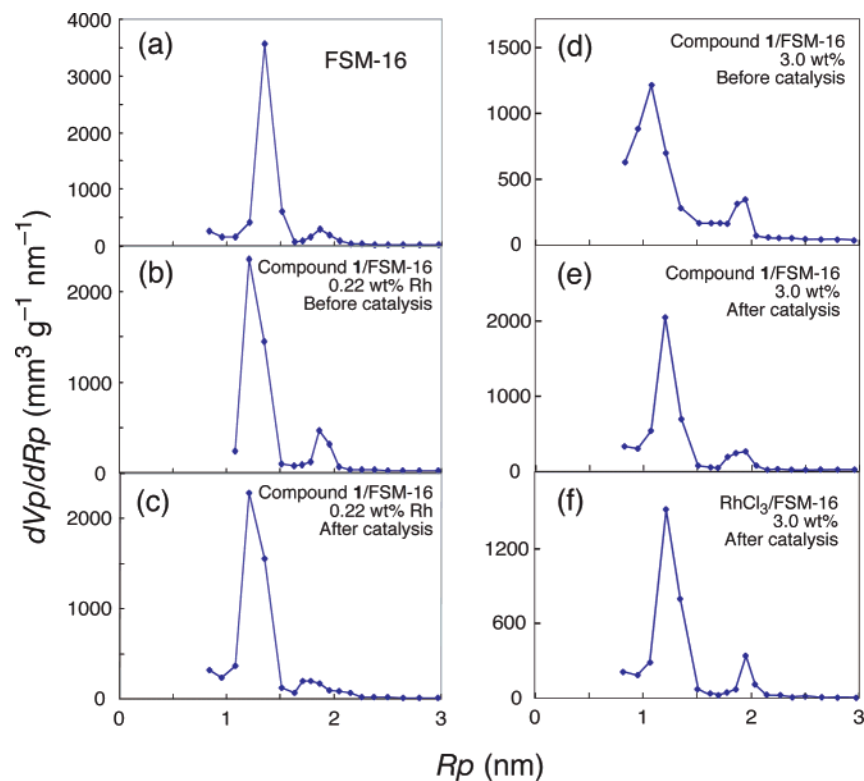
Figure 2. Pore size distribution base on DH-plot method for the sorption and desorption isotherms for (a) FSM-16, [RhMo$_6$O$_{18}$(OH)$_6$]$^{3-}$/FSM-16 catalysts [(b, c) 0.22 and (d, e) 3.0 wt % Rh], before (b, d) and after (c, e) the propene hydroformylation at 433 K for 5 h, and (f) RhCl$_3$/FSM-16 catalyst (3.0 wt % Rh) after propene hydroformylation.
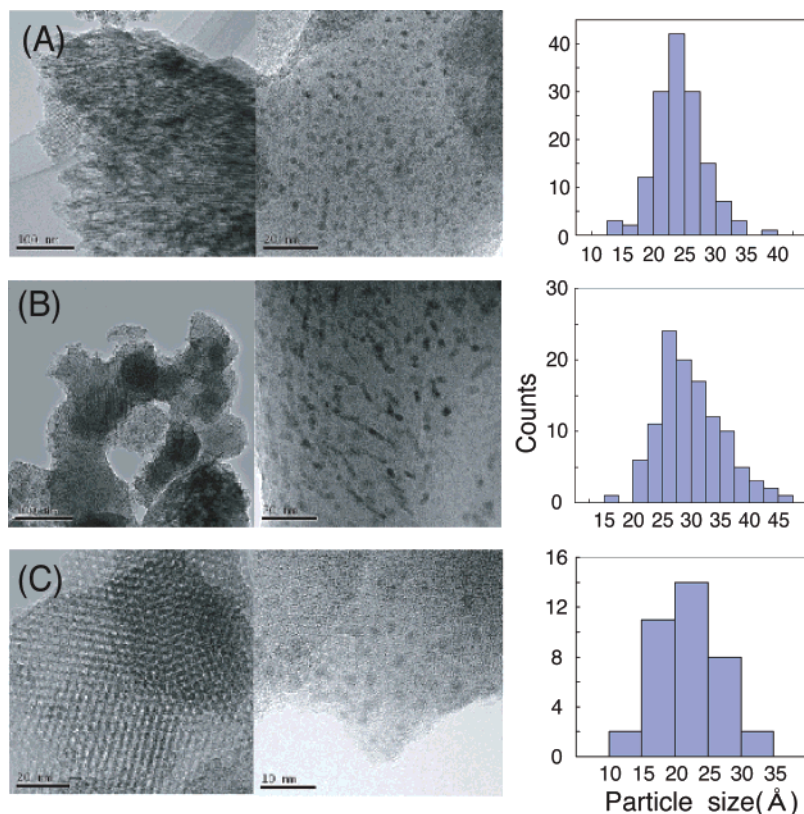

Figure 3. High-resolution TEM image and particle size distribution histogram for [RhMo$_6$O$_{18}$(OH)$_6$]$^{3-}$/FSM-16 catalyst (3.0 wt % Rh) before (A) and after (B) propene hydroformylation reaction at 433 K for 5 h and for the RhCl$_3$/FSM-16 catalyst (0.5 wt % Rh) after hydroformylation (C).

transform of the Rh K-edge EXAFS before catalytic tests. This peak was due to the Rh−O bonds at 1.88−2.03 Å (Table 4, part A). The central hetero Rh atom constitutes octahedral coordination with six bridging oxygen atoms in crystal **1**. The

N value for Rh−O bonds was 6.2−7.0. The Rh(−O−)Mo peak intensity appeared at 3.0 Å and progressively decreased as the Rh amount decreased from 5.2 to 0.22 wt % (Figure S1, part B, spectra a1, b1, and c1). The Rh−O and Rh(−O−)Mo bond

TABLE 4: Best Fit Results to Rhodium K-edge EXAFS for Various Rhodium−Molybdenum Catalysts Supported in/on FSM-16 and Reference Rh Catalysts

Rh wt %	Rh−O		Rh−C		Rh(−C−)C		Rh−Rh or Rh−Mo		Rh(−O−)Mo		goodness of fit
	N	R(Å)	N	R(Å)	N	R(Å)	N	R(Å)	N	R(Å)	
(A) Before Hydroformylation											
[RhMo$_6$O$_{18}$(OH)$_6$]$^{3-}$/FSM-16											
0.22	6.6	1.88									12350
3.0	6.2	2.014							4.2	3.34	1138
5.2	7.0	2.030							5.3	3.35	5829
[Rh(COD)$_2$]$^+$−[AlMo$_6$O$_{18}$(OH)$_6$]$^{3-}$/FSM-16											
1.6	1.8	2.05	8.0[b]	2.092	8.0[b]	2.962					140
[Rh(COD)$_2$]$^+$/FSM-16											
1.1	2.0	2.04	8.0[b]	2.09	8.0[b]	2.99					404
(B) After Hydroformylation (433 K, 5 h)[a]											
[RhMo$_6$O$_{18}$(OH)$_6$]$^{3-}$/FSM-16											
0.22							8.4	2.679			1674
3.0	5.2	2.028					1.6	2.709	0.8	3.37	48
5.2	4.0	2.041					1.3	2.676	1.0	3.364	187
[Rh(COD)$_2$]$^+$−[AlMo$_6$O$_{18}$(OH)$_6$]$^{3-}$/FSM-16											
1.6							8.2	2.688			1567
RhCl$_3$/FSM-16											
0.5							7.3	2.686			2074
33							7.7	2.685			2431
crystal **1**	6	2.021							6	3.355	ref 19
crystal **3**			8	2.228	8	3.043					ref 18

[a] Initial total gas pressure 60.0 kPa; propene/CO/H$_2$ = 1:1:1. [b] Equalized to the values for [Rh(COD)$_2$]$^+$[BF$_4$]$^-$ because no loss of COD ligand was found during catalyst synthesis (UV−visible absorption) and pretreatment (GC).

TABLE 5: Best Fit Results to Molybdenum K-edge EXAFS for Various Rhodium−Molybdenum Catalysts Supported in/on FSM-16 and Reference Rh Catalysts

Rh wt %	Mo−O		Mo−O		Mo−Rh		Mo(−O−)Mo or Mo(−O−)Rh		goodness of fit
	N	R(Å)	N	R(Å)	N	R(Å)	N	R(Å)	
(A) Before Hydroformylation									
[RhMo$_6$O$_{18}$(OH)$_6$]$^{3-}$/FSM-16									
0.22	6.1	1.60	1.3	2.07			4.0	3.41	1680
3.0	0.6	1.67	1.1	2.00			2.5	3.356	1955
[Rh(COD)$_2$]$^+$−[AlMo$_6$O$_{18}$(OH)$_6$]$^{3-}$/FSM-16									
1.6	1.6	1.664	1.9	1.99			2.2	3.324	425
(B) After Hydroformylation (433 K, 5 h)[a]									
[RhMo$_6$O$_{18}$(OH)$_6$]$^{3-}$/FSM-16									
0.22	1.0	1.664	5.3	1.98	0.9	2.74	1.4	3.185	17
3.0	1.8	1.66	2.4	1.99	1.5	2.59			3.0
5.2	0.7	1.67	4.7	1.94	1.4	2.56	0.8	3.35	993
[Rh(COD)$_2$]$^+$−[AlMo$_6$O$_{18}$(OH)$_6$]$^{3-}$/FSM-16									
1.6	1.7	1.66	2.8	1.89	0.2	2.563	1.3	3.286	203
crystal **1**	4	1.825	2	2.289			3	3.366	ref 19

[a] Initial total gas pressure 60.0 kPa; propene/CO/H$_2$ = 1:1:1.

distances were comparable to the values for crystal **1** (Table 4). No Rh(−O−)Mo peak was observed for the sample of 0.22 wt % Rh.

For the catalysts after the hydroformylation reaction, a new peak at 2.4 Å appeared commonly in Figure S1, part B, spectra a2, b2, and c2. The peak was fit well as a metallic Rh−Rh bond at 2.676−2.709 Å with N values of 1.3−8.4 (Table 4, part B). Note that metallic Rh−Rh and Rh−Mo (see the Mo K-edge EXAFS section) bonds were not separated in the Rh K-edge EXAFS, and thus the peak may include the contribution of metallic Rh−Mo bonds. These peak positions were essentially identical to those for a single peak due to Rh−Rh bonding in the Fourier transform for RhCl$_3$/FSM-16 after hydroformylation tests (2.685−2.686 Å, Figure S1, part B, spectrum f2 and Table 4, part B). Metallic Rh nanoparticles were formed under the catalytic conditions.

For [RhMo$_6$O$_{18}$(OH)$_6$]$^{3-}$/FSM-16 (3.0 and 5.2 wt % Rh) catalysts after catalysis, two peaks were observed at 1.6 and 3.1 Å in the Fourier transform (Figure S1, part B, spectra b2

and c2) in addition to the Rh−Rh (and/or Rh−Mo) bonding. The two peaks were fit well as Rh−O and Rh(−O−)Mo bonds at 2.028−2.041 Å (N = 4.0 − 5.2) and 3.36−3.37 Å (N = 0.8−1.0) (Table 4, part B), comparable to values before catalysis (Table 4, part A). The N values decreased to 57−84% for Rh−O bonds and 19% for Rh(−O−)Mo bonds compared to those before catalysis. Thus, a part of compound **1** anions remained in samples of 3.0−5.2 wt % Rh after catalytic tests. The heteropolyacid molecules (and/or distorted ones) and aggregated metallic nanoparticles coexisted.

For [Rh(COD)$_2$]$^+$−[AlMo$_6$O$_{18}$(OH)$_6$]$^{3-}$/FSM-16 before the catalytic test, the bonds of Rh−C (2.092 Å) and Rh(−C−)C (2.962 Å) corresponded to values for crystal **3** (Table 4). The two COD coordination was distorted but intact upon supporting. New Rh−O bonds were formed at 2.05 Å with an N value of 1.8. For [Rh(COD)$_2$]$^+$/FSM-16 before hydroformylation (Table 4, part A), two COD ligands seem retained based on Rh−C (2.09 Å) and Rh(−C−)C bonds (2.99 Å). In addition, two Rh−O bonds were formed at 2.04 Å (Table 4, part A). A clear

difference in the presence/absence of compound **2** was not found in the Rh K-edge EXAFS.

After hydroformylation, the Rh K-edge EXAFS spectra for the $[Rh(COD)_2]^+-[AlMo_6O_{18}(OH)_6]^{3-}$/FSM-16 catalyst (Figure S1, spectra d2) became similar to that for $[RhMo_6O_{18}(OH)_6]^{3-}$/FSM-16 (0.22 wt % Rh, Figure S1, spectra a2) or RhCl$_3$/FSM-16 (Figure S1, spectra f2). The best-fit values for the Rh−Rh (and/or Rh−Mo) bonds were at 2.688 Å with the N value of 8.2 (Table 4, part B). No Rh−O or Rh(−O−)Mo peaks were detected in contrast to data for $[RhMo_6O_{18}(OH)_6]^{3-}$/FSM-16 catalysts. Therefore, the Al sites of $[AlMo_6O_{18}(OH)_6]^{3-}$/FSM-16 were not replaced with the Rh cations of $[Rh(COD)_2]^+$.

b. Mo K-Edge. The Mo K-edge EXAFS data for $[RhMo_6O_{18}(OH)_6]^{3-}$/FSM-16 (0.22−3.0 wt % Rh) before catalysis required three shells (two Mo−O and one Mo(−O−)Mo) for reasonable fit. The best-fit data were shorter Mo−O bonds at 1.60−1.67 Å with N values of 0.6−6.1, longer Mo−O bonds at 2.00−2.07 Å with N values of 1.1−1.3, and Mo(−O−)Mo (or Mo(−O−)Rh) bonds at 3.36−3.41 Å with N values of 2.5−4.0. The deviations for Mo−O bonds were relatively greater compared to the corresponding data for crystal **1** (Table 5).

For $[RhMo_6O_{18}(OH)_6]^{3-}$/FSM-16 (0.22−5.2 wt % Rh) after catalytic tests, two Mo−O peaks remained at 1.66−1.67 and 1.94−1.99 Å (Table 5, part B). The peak due to Mo(−O−)Mo or Mo(−O−)Rh bonds (3.19−3.35 Å) became weaker (0.22 and 5.2 wt % Rh; Figure S2, part B, spectra a2 and c2) or undetectable (3.0 wt % Rh, Figure S2, part B, spectrum b2). In addition, a new peak appeared at 3.3−3.6 Å (Figure S2, part B, spectra a2, b2, and c2). The peak was fit well as metallic Mo−Rh bonds at 2.56−2.74 Å (Table 5, part B) with N values 0.9−1.5.

The Mo K-edge EXAFS spectra for $[Rh(COD)_2]^+-[AlMo_6O_{18}(OH)_6]^{3-}$/FSM-16 catalyst before hydroformylation (Figure S2, spectra d1) were similar to those for crystal **2** and incipient $[RhMo_6O_{18}(OH)_6]^{3-}$/FSM-16 (Figure S2, spectra b1). The data was best fit with three shells of two Mo−O and one Mo(−O−)Mo (Table 5, part A). The bond distances were comparable to those for crystal **1** and the N value was 40−95% of the corresponding values for crystal **1**.

After the catalysis, a new peak appeared at 2.3 Å (Figure S2, part B, spectrum d2) due to metallic Mo−Rh bonds in addition to three bonds derived from a Mo oxide species. The bond distance was determined to 2.563 Å with an N value of 0.2 (Table 5, part B).

Discussion

Selective Butanol Synthesis. The propene hydroformylation reaction has been studied over supported Rh catalysts. Under 101 kPa at 400 K over Rh/silica-gel prepared from rhodium chloride, the major product was propane (46%) in addition to *i*-butanal (35%) and *n*-butanal (19%).[22] At 400−423 K over Rh−Y zeolite catalysts, the products were propane (64−97%) and minor butanals.[22,23] Under 101 kPa at 418 K over Mo−Rh/SiO$_2$ catalysts prepared via subsequent impregnation of rhodium chloride and ammonium heptamolybdate, the major products were butanols (27−39%) and propane (61−67%).[12] A similar product distribution was reported for the catalyst prepared from Cp$_3$RhMo$_2$(CO)$_5$ (Cp = cyclopenetadiene) on SiO$_2$.[13]

The formation of *n*-butanol was superior over $[RhMo_6O_{18}(OH)_6]^{3-}$/FSM-16 (60−97 mol %) and RhCl$_3$/FSM-16 catalysts (25−73 mol %) to *i*-butanol 0−38 and 0−21 mol %, respectively. Selection to the *n*-form was in accord with refs 12 and 13. Selective alcohol formation (94−100%) was reported in the

hydroformylation of 1-hexene using homogeneous RhH(PEt$_3$)$_3$ or Rh$_2$OAc$_4$(PPh$_3$)$_3$ in ethanol at 3.0−6.6 MPa and 393 K.[24]

The butanols selectivity over $[RhMo_6O_{18}(OH)_6]^{3-}$/FSM-16 (60−98 mol %) was high under milder condition at 60 kPa and 433 K (Table 3). The butanols selectivity (46−73 mol %) over RhCl$_3$/FSM-16 was comparable to Mo−Rh binary catalysts on SiO$_2$.[12,13] In this context, mesoporous reaction space seems the primary control factor to selectively form butanols. As the Rh (and Mo) loading amount decreased, butanol selectivity increased over both $[RhMo_6O_{18}(OH)_6]^{3-}$/FSM-16 and RhCl$_3$/FSM-16 catalysts. In the comparison of identical Rh loading amounts of $[RhMo_6O_{18}(OH)_6]^{3-}$/FSM-16 and RhCl$_3$/FSM-16 catalysts (3.0 wt %), the butanols selectivity was 97 and 52 mol %, respectively. Thus, the presence of Mo additionally affected the formation to be more selective to butanol.

Active Sites for Selective Butanol Synthesis. *a. Incipient Supported Structure.* The mesoporous framework of FSM-16 is basically retained upon supporting crystals **1**−**3** and after the propene hydroformylation reaction at 433 K for 5 h based on the (100)-reflection XRD peak and TEM images (Table 1 and Figures 2 and 3). The d_{100} spacing expanded by 1.6−5.4% for Rh[−Mo]/FSM-16 catalysts compared to native FSM-16 (Table 1). A hexagonal symmetric structure was observed (parts A−C of Figure 3).

The incipient supported structure of $[RhMo_6O_{18}(OH)_6]^{3-}$ in/on FSM-16 was studied by Rh and Mo K-edge EXAFS. On the basis of the Rh−O bond distances and the N values (Table 4, part A), the octahedral central Rh cation was retained. The presence of Rh(−O−)Mo bonds demonstrated that the heteropolyacid framework was retained in the cases of 3.0−5.2 wt % Rh. The peak was not observed for $[RhMo_6O_{18}(OH)_6]^{3-}$/FSM-16 with 0.22 wt % Rh. A smaller amount of the anions may interact more effectively with the surface of FSM-16 and distort more. The deviation of fit data (bond distance and the N value) for Mo−O bonds were relatively greater than those for Rh−O, Rh(−O−)Mo, or Mo(−O−)Mo/Rh bonds compared to data for crystal **1** (Tables 4 and 5). The hydroxyl and/or oxo group(s) bound to the Mo atoms of compound **1** anion may be interacting with the surface of FSM-16.

On the basis of Mo K-edge EXAFS, the framework of $[AlMo_6O_{18}(OH)_6]^{3-}$ was demonstrated to remain; however, local structure around the Mo−O bonds was more distorted (Table 5, part A) than for Mo(−O−)Mo bonds, similar to the case of supported $[RhMo_6O_{18}(OH)_6]^{3-}$. On the basis of Rh K-edge EXAFS, two COD ligands per one Rh cation were distorted upon supporting and the Rh cation was bound via about two oxygen atoms for the $[Rh(COD)_2]^+-[AlMo_6O_{18}(OH)_6]^{3-}$/FSM-16 catalyst (Table 4, part A). Because very similar fit results were obtained for $[Rh(COD)_2]^+$/FSM-16 and the Rh loading was greater for $[Rh(COD)_2]^+-[AlMo_6O_{18}(OH)_6]^{3-}$/FSM-16 (1.6 wt % Rh) than 1.1 wt % Rh for $[Rh(COD)_2]^+$/FSM-16, the $[Rh(COD)_2]^+$ cations should be immobilized with both surface O/OH groups of FSM-16 and $[AlMo_6O_{18}(OH)_6]^{3-}$ dispersed in/on FSM-16.

b. Structure during/after Hydroformylation. After the propene hydroformylation at 433 K for 5 h, the Rh site structure changed in all the Rh[−Mo]/FSM-16 catalysts studied. The Rh cations aggregated to form metallic Rh nanoparticles based on the Rh−Rh bonds for the $[RhMo_6O_{18}(OH)_6]^{3-}$/FSM-16 catalyst with 0.22 wt % Rh (Table 4, part B). As the Rh loading amount increased to 5.2 wt %, the N values for Rh−Rh bonding gradually decreased and those for Rh−O and Rh(−O−)Mo derived from the remaining/distorted Rh heteropolyacid anions increased.
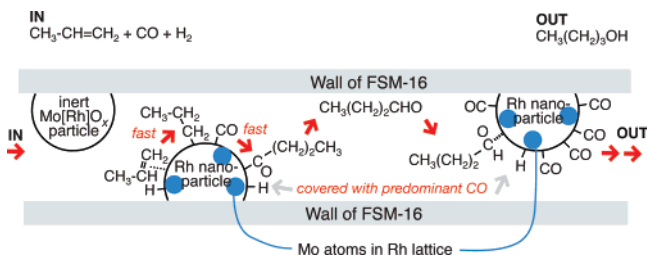
Figure 4. Proposed mechanism of selective *n*-butanol synthesis over $[RhMo_6O_{18}(OH)_6]^{3-}$/FSM-16 catalysts.

In the Mo K-edge EXAFS, metallic Mo−Rh bonds were observed at 2.56−2.74 Å with *N* values of 0.9−1.5 in addition to Mo−O and Mo(−O−)Mo/Rh bonds. Because the Mo(VI) site is difficult to be reduced to metallic Mo nanoparticles in propene + CO + H_2 at 433 K, the Mo−Rh bonds should be derived from alloylike Mo sites included in/on metallic Rh nanoparticle lattices. The face-centered cubic and body-centered cubic crystal phases were reported for the Mo_xRh_{100-x} alloy (*x* = 10, 26, 35, and 65).[25] The $MoRh_3$ alloy on SiO_2 was detected by XRD,[26] and Mo−Rh alloy crystal phases were observed by TEM.[27] In summary, Rh sites constituted metallic nanoparticles mixed with Mo atoms and the rest of the Mo sites constituted Mo oxide and/or Mo−Rh binary oxide phases. The ratio of Mo[−Rh] oxide phase(s) increased as the metal loading increased.

For $[Rh(COD)_2]^+$−$[AlMo_6O_{18}(OH)_6]^{3-}$/FSM-16 and $RhCl_3$/FSM-16 catalysts after catalytic tests, the Rh nanoparticles were predominantly formed based on a single Rh−Rh peak in the Rh K-edge EXAFS (Table 4). The interaction between Rh and the MoO_x species should be weak based on the absence of Rh−O and Rh(−O−)Mo bonds. A Mo−Rh bond(s) was observed in the Mo K-edge EXAFS for $[Rh(COD)_2]^+$−$[AlMo_6O_{18}(OH)_6]^{3-}$/FSM-16 (Table 5), but the *N* value was only 0.2 compared to 0.9−1.5 for $[RhMo_6O_{18}(OH)_6]^{3-}$/FSM-16 catalysts. Therefore, the population of alloylike Rh−Mo particle sites were smaller in the catalyst. Rh and Mo atoms were easier to mix as alloylike nanoparticles starting from $[RhMo_6O_{18}(OH)_6]^{3-}$ rather than from separate molecules of $[Rh(COD)_2]^+$ and $[AlMo_6O_{18}(OH)_6]^{3-}$.

Implications to Butanol Synthesis Mechanism. Aldehydes are predominantly produced in homogeneous-phase hydro-formylation[1] because the Rh centers are often coordinated with multiple CO ligands to preferably proceed CO insertion.[28] Metallic nanoparticles were formed in all the catalysts in this work (Table 4). The relatively small Rh[−Mo] nanoparticle confined in the FSM-16 mesopore may be predominantly adsorbed with CO to be selective toward oxygenates (Figure 4). The diffusion of reactants and intermediates was relatively slow in the two-dimensional mesospace compared to that over the amorphous silica gel surface. Thus, multiple-step hydrogenations of intermediate aldehydes should proceed for Rh/FSM-16 catalysts in this work (Figure 4). Similar diffusion effects in microporous space were reported for the regioselective hydrogenation over Rh clusters in NaY and chemo-selective hydrogenation over Pt or Rh clusters in NaY.[29]

Selective *n*-butanol synthesis (Table 3, entries a−d) was in accord with the predominant *n*-butanol among oxygenate compounds over Mo−Rh/SiO_2 catalysts.[12,13] However, propane formation was not promoted by the addition of Mo in Table 3 in clear contrast to promoted formation of *n*-butanol and propane over Mo−Rh/SiO_2 catalysts.[12,13]

First, the Rh[−Mo] particle size is considered. The size was 24−28 Å for $[RhMo_6O_{18}(OH)_6]^{3-}$/FSM-16 catalysts affected

by the regular pore opening of 27 Å for FSM-16 (Table 1 and Figure 3). The mean size varied between 19 and 42 Å for Mo−Rh/SiO_2 catalysts as a function of Mo/Rh atomic ratio (0.2−1), but the butanols selectivity did not significantly change (27−39%)[12] compared to 60−98% for $[RhMo_6O_{18}(OH)_6]^{3-}$/FSM-16 (Table 3, part A). Thus, a different trend to propane was not ascribed only to the Rh[−Mo] particle size difference.

Next, the contact between Mo and Rh is considered. The Mo atoms were demonstrated in/on the Rh nanoparticle lattice based on the Mo−Rh peak at 2.56−2.74 Å (Table 5, part B). Direct metallic Mo−Rh bonding was confirmed for the first time for Mo-promoted Rh nanoparticle catalysts. Mo−Rh alloy dispersed on SiO_2 was already demonstrated by XRD[26] and TEM.[27] A reference $[AlMo_6O_{18}(OH)_6]^{3-}$/FSM-16 catalyst exhibited negligible catalytic activity in propene hydroformylation and no Mo−Al peak was observed in the Mo K-edge EXAFS after the catalytic test. For $[Rh(COD)_2]^+$−$[AlMo_6O_{18}(OH)_6]^{3-}$/FSM-16, the *N* value of Mo−Rh bonds was only 0.2. Thus, Rh nanoparticles atomically mixed with Mo atoms were active, and inert Mo oxide species coexisted.

We propose that CO insertion predominantly proceeded on the Rh−Mo nanoparticles dominated with adsorbed CO, and hydrogenations of alkyl and aldehyde intermediates were suppressed on the Rh ensemble segregated by Mo atoms (Figure 4). In sacrifice of total conversion (0.13−0.52%, Table 3, part A) over $[RhMo_6O_{18}(OH)_6]^{3-}$/FSM-16, butanols were selectively produced during slow, rate-limiting diffusion in a two-dimensional mesopore. The propyl intermediate may quickly react with CO to form an acyl intermediate (Figure 4). Hence, propane formation was negligible on the catalysts (Table 3).

An alloylike site may be easier to be formed with the greater Mo/Rh atomic ratio 6 for $[RhMo_6O_{18}(OH)_6]^{3-}$/FSM-16 compared to 0.2−2 for Mo−Rh/SiO_2 catalysts.[12,13] Atomically mixed Mo sites on/in Rh nanoparticles were more easily formed starting from compound **1** rather than compounds **2** + **3** (Tables 4 and 5). In fact, both propane and butanols were formed on $[Rh(COD)_2]^+$−$[AlMo_6O_{18}(OH)_6]^{3-}$/FSM-16 (Table 3, entry e). The alloylike Zn−Rh ensemble was suggested on SiO_2 based on infrared absorption spectroscopy for adsorbed CO. CO insertion was enhanced in contrast to the remarkable suppression of hydrogenation over segregated Rh sites by Zn atoms.[30,31] Similarly, Rh sites were segregated by Sn atoms to be selective for hydrogenation and hydrogenolysis.[32]

Patchlike transition metal suboxide or cationic sites (Ti,[33] V,[12,34] Mn,[35−37] Fe,[12,38] Zr,[30] Nb,[39] or Mo[12,13,35,40]) were proposed to cover Rh nanoparticles dispersed on SiO_2. The Rh sites covered with patchlike MoO_x may retain hydrogenation activity of alkyl and aldehyde intermediates in Mo−Rh/SiO_2 catalysts.[12,13] The promotion of both propane and alcohol synthesis was also reported for Rh nanoparticles in contact with $Fe^{\delta+}$.[38]

In summary, two control factors were proposed in combination for selective butanol synthesis: the two-dimensional space of FSM-16 to lead to slower diffusion of oxygenate intermediates and Rh nanoparticles atomically mixed with Mo. The selectivity to butanols versus propane increased in the order $[RhMo_6O_{18}(OH)_6]^{3-}$/FSM-16 (2-D diffusion and atomically mixed Rh−Mo) > $RhCl_3$/FSM-16 (2-D diffusion) > Mo−Rh/SiO_2[12,13] ≫ Rh/SiO_2. The effect of the remaining Cl (0.22−0.28 wt %, Table 1) cannot be excluded for $RhCl_3$/FSM-16.

The reason is unclear why the butanol selectivity increased as the Rh loading amount decreased both in the $[RhMo_6O_{18}(OH)_6]^{3-}$/FSM-16 and in the $RhCl_3$/FSM-16 catalysts. The mixing ratio of atomic Mo with Rh may change as a function

Butanol Synthesis over Rh—Mo Catalysts in FSM-16 ·
J. Phys. Chem. C, Vol. 111, No. 27, 2007 **10081**

of metal loading, as suggested by the variation of N values for Mo—Rh bonds (0.9—1.5, Table 5, part B).

Finally, the population of Rh[—Mo] metal particles and Mo[—Rh] oxide particles inside and outside the FSM-16 framework should be mentioned. On the basis of the relatively narrow particle size distribution centered at 22—28 Å (Figure 3 and Table 1), these particles could grow up to the internal size limit of 27 Å in the catalyst impregnation steps (Figure 3A). A particle size increase of 4—6 Å as the metal loading increases or after hydroformylation suggests that extra Rh/Mo species may grow also on the external surface of the FSM-16 crystalline. These trends are consistent with catalytic results that the multiple-step product butanols were more selectively formed as the metal loading progressively decreased and the population of Rh/Mo inside mesopore was greater (Table 3).

Conclusions

Selective butanol synthesis catalysts (60—98 mol %) were found in propene hydroformylation at 433 K and 60 kPa prepared from $[RhMo_6O_{18}(OH)_6]^{3-}$ crystals and FSM-16. Rh nanoparticles ($\approx$23 Å) in the mesopores were essential for the selective synthesis. Because of the slow diffusion in the mesopore, oxygenate intermediates were subject to multiple-step hydrogenations to convert finally to *n*-butanol. Additionally, Mo atomically mixed in/on Rh nanoparticles was suggested to segregate the surface Rh ensemble and be further selective for CO insertion. The Mo—Rh coordination based on Mo K-edge EXAFS was the key to indicate the Mo—Rh alloy formation and selective formation of *n*-butanol. The coordination number was smaller/zero for catalysts prepared from $[AlMo_6O_{18}(OH)_6]^{3-}$ and/or $[Rh(COD)_2]^+$ crystals over FSM-16, and the catalysis was not selective to butanol.

Supporting Information Available: Data and best fit results of Rh K-edge and Mo K-edge EXAFS. This material is available free of charge via the Internet at http://pubs.acs.org.

References and Notes

(1) Cole-Hamilton, D. J. *Science* **2003**, *299*, 1702—1706.
(2) Mukhopadhyay, K.; Mandale, A. B.; Chaudhari, R. V. *Chem. Mater.* **2003**, *15*, 1766—1777.
(3) Huang, L.; Kawi, S. *Bull. Chem. Soc. Jpn.* **2004**, *77*, 295—302.
(4) Yang, Y.; Lin, H.; Deng, C.; She, J.; Yuan, Y. *Chem. Lett.* **2005**, *34* (2), 220—221.
(5) Marteel, A. E.; Tack, T. T.; Bektesevic, S.; Davies, J. A.; Mason, M. R.; Abraham, M. A. *Environ. Sci. Technol.* **2003**, *37* (23), 5424—5431.
(6) Nomiya, K.; Takahashi, T.; Shirai, T.; Niwa, M. *Polyhedron* **1987**, *6* (2), 213—218.
(7) Ali, B. E.; Tijani, J.; Fettouhi, M.; Al-Arfaj, A. *Appl. Catal., A* **2005**, *283*, 185—196.
(8) Zsigmond, A.; Bogar, K.; Notheisz, F. *J. Catal.* **2003**, *213*, 103—108.
(9) Kozhevnikov, I. V.; Kloetstra, K. R.; Sinnema, A.; Zandbergen, H. W.; Bekkum, v. H. *J. Mol. Catal.: A* **1996**, *114*, 287—298.
(10) Augustine, R. L.; Goel, P.; Mahata, N.; Reyes, C.; Tanielyan, S. K. *J. Mol. Catal.: A* **2004**, *216*, 189—197.
(11) Bianchini, C.; Barbaro, P. *Top. Catal.* **2002**, *19* (1), 17—32.
(12) Tomishige, K.; Furikado, I.; Yamagishi, T.; Ito, S.; Kunimori, K. *Catal. Lett.* **2005**, *103* (1—2), 15—21.
(13) Trunschke, A.; Böttecher, H. C.; Fukuoka, A.; Ichikawa, M.; Miessner, H. *Catal. Lett.* **1991**, *8*, 221—228.
(14) Shenck, T. G.; Downs, J. M.; Milne, C. R. C.; Mackenzie, P. B.; Boucher, H.; Whealan, J.; Bosnich, B. *Inorg. Chem.* **1985**, *24*, 2334—2337.
(15) Nomura, M.; Koike, Y.; Sato, M.; Koyama, A.; Inada, Y.; Asakura, K. In *X-Ray Absorption Fine Structure- XAFS13: 13th International Conference*; Proceedings of the International Conference on X-ray and Absorption Fine Structure, Stanford, CA, July 9—14, 2006; Hedman, B., Pianetta, P., Eds.; American Institute of Physics: Melville, NY, 2007; , Vol. 882, pp 896—898.
(16) Bearden, J. A. *Rev. Mod. Phys.* **1967**, *39*, 78—124.
(17) Wells, A. F. *Structural Inorganic Chemistry*, 5th ed.; Clarendon Press: Oxford, U.K., 1984.
(18) Shenck, T. G.; Downs, J. M.; Milne, C. R. C.; Mackenzie, P. B.; Boucher, H.; Whealan, J.; Bosnich, B. *Inorg. Chem.* **1985**, *24*, 2334—2337.
(19) Ozawa, Y.; Hayashi, Y.; Isobe, K. *Acta. Crystallogr.* **1991**, *C47*, 637—638.
(20) Gatehouse, B. M.; Leverett, P. *J. Chem. Soc. A* **1969**, 849—854.
(21) Ankudinov, A. L.; Ravel, B.; Rehr, J. J.; Conradson, S. D. *Phys. Rev. B* **1998**, *58*, 7565—7576.
(22) Takahashi, N.; Kobayashi, M. *J. Catal.* **1984**, *85*, 89—97.
(23) Arai, H.; Tominaga, H. *J. Catal.* **1982**, *75*, 188—189.
(24) MacDougall, J. K.; Cole-Hamilton, D. J. *J. Chem. Soc., Chem. Commun.* **1990**, 165—167.
(25) Gürler, R. *J. Mater. Sci. Lett.* **1999**, *18*, 445—447.
(26) Kunimori, K.; Wakasugi, T.; Yamakawa, F.; Oyanagi, H.; Nakamura, J.; Uchijima, T. *Catal. Lett.* **1991**, *9*, 331—338.
(27) Lamber, R.; Jaeger, N. I.; Trunschke, A.; Miessner, H. *Catal. Lett.* **1991**, *11*, 1—10.
(28) Shriver, D.; Atkins, P. *Inorganic Chemistry*, 4th ed.; Oxford University Press: Oxford, U.K., 2006.
(29) Creyghton, E. J.; Downing, R. S. *J. Mol. Catal. A* **1998**, *134*, 47—61.
(30) Sachtler, W. M. H.; Ichikawa, M. *J. Phys. Chem.* **1986**, *90* (20), 4752—4758.
(31) Jen, H. W.; Zheng, Y.; Schriver, D. F.; Sachtler, W. M. H. *J. Catal.* **1989**, *116*, 361—372.
(32) Candy, J. P.; Didillon, B.; Smith, E. L.; Shay, T. B.; Basset, J. M. *J. Mol. Catal.* **1994**, *86*, 179—204.
(33) Levin, M. E.; Salmeron, M.; Bell, A. T.; Somorjai, G. A. *J. Chem. Soc., Faraday Trans. 1* **1987**, *83*, 2061—2069.
(34) Lee, G. v. d.; Ponec, V. *Catal. Rev. Sci. Eng.* **1987**, *29*, 183—218.
(35) van der Berg, F. G. A.; Glezer, J. H. E.; Sachtler, W. M. H. *J. Catal.* **1985**, *93*, 340—352.
(36) Treviño, H.; Hyeon, T.; Sachtler, W. M. H. *J. Catal.* **1997**, *170*, 236—243.
(37) Ichikawa, M.; Hoffmann, P. E.; Fukuoka, A. *J. Chem. Soc., Chem. Commun.* **1989**, 1395—1396.
(38) Ichikawa, M. *Polyhedron* **1988**, *7* (22—23), 2351—2367.
(39) Yoshitake, H.; Asakura, K.; Iwasawa, Y. *J. Chem. Soc., Faraday Trans. 1* **1988**, *84*, 4337—4346.
(40) Wardinsky, M. D.; Hecker, W. C. *J. Phys. Chem.* **1988**, *92*, 2602—2604.